ORGANIC CHEMISTRY FRONTIERS

RESEARCH ARTICLE

View Article Online
View Journal

Cite this: DOI: 10.1039/d5qo00698h

A new fully bridged spirophenylacridine derivative: synthesis and characterization†

Shi-Jie Ge, ‡[a] Yue-Jian Yang,‡[a] Rui-Hong Liu,[a] You-Jun Yu,[a] Rehman-Mehvish Abdul,[a] Hai-Xiao Jiang,[b] Wei Gao,[a] Dong-Ying Zhou [a] and Zuo-Quan Jiang *[a]

Received 29th April 2025,
Accepted 24th June 2025

DOI: 10.1039/d5qo00698h

rsc.li/frontiers-organic

A new spirophenylacridine (SPA) derivative, SPA-SO2, was synthesized *via* full bridging of sulfone, carbonyl, and oxygen to the SPA core. Using its precursor molecule SPA-S as a reference, the two molecules were systematically characterized, including single crystal structures, electrochemical properties, and photophysical properties. Notably, SPA-SO2 exhibits a blue shift and narrowing of spectra compared to SPA-S. Theoretical investigations provided mechanistic insights, suggesting that bridging modifications can precisely modulate molecular properties by altering the electronic structure. Finally, SPA-SO2 was applied in electroluminescence devices, exhibiting deep blue emission at 436 nm and achieving a maximum external quantum efficiency of 9.4%. This work introduces a bridging modification strategy for SPA, contributing to advancements in optoelectronic materials.

1 Introduction

The unique stereochemical configuration of spiro compounds endows them with remarkable advantages in enriching functionality through molecular modifications.[1–8] As a classic spiro block, 9,9′-spirobifluorene can be further derivatized by incorporating a heteroatom, as shown in Fig. 1a.[9,10] These compounds are characterized by a sp^3-hybridized carbon atom at the core of the spiro structure, which enables the spatial extension of two distinct π-systems in an orthogonal orientation. Among these, the fusion of an amine with the spiro structure has sparked broader interest in spirophenylacridine (SPA) because of its potential to generate numerous subtypes.[11–16] To be specific, the bay areas introduced by an amine further enhanced the tunability and functionalization of the molecule (Fig. 1b). As a result, it has been widely applied in organic light-emitting diodes, organic photovoltaics, and perovskite solar cells.[17–25]

Bridging heteroatoms or functional groups in bay areas has proven to be an effective strategy for modulating electronic structures and photophysical characteristics.[26–29] Since the spiro carbon atom of SPA is connected to different π-systems, modifications can be independently performed on the amine moiety and the other segment of the spiro structure (Fig. 1b). On the one hand, modifications can be made by bridging the bay areas of the amine fragment. In 2016, our research group introduced an oxygen atom at the bay area of the amine unit, enhancing its electron-donating ability and lowering the energy of the singlet (S_1) excited state.[30] At the same time, Poriel's group employed sulfur modification at the same position, which not only raised the highest occupied molecular orbital (HOMO) energy level but also enhanced the molecule's spin–orbit coupling properties.[31] In 2023, our group further rigidified the molecular backbone by introducing carbonyl groups at both bay positions, thereby suppressing molecular vibrations and improving the photoluminescence quantum yield (PLQY).[32] On the other hand, a heteroatom or functional group can be further bridged into another segment of the spiro structure. For instance, Lee and coworkers bridged sulfur, oxygen, and aniline units into this segment, enabling precise modulation of the molecular dipole moment, which in turn led to distinct photoluminescence efficiencies in solid thin films.[33] These studies suggest that bridging modifications of SPA using heteroatoms or functional groups can effectively modulate the properties of the molecules and are worthy of further investigation.

In this work, we report a new derivative of SPA, designated as SPA-SO2, in which sulfone, carbonyl, and oxygen are fully bridged on the SPA core (Fig. 1c). For comparison, the characteristics of its precursor molecule SPA-S were investigated

[a]*State Key Laboratory of Bioinspired Interfacial Materials Science, Institute of Functional Nano & Soft Materials (FUNSOM), Soochow University, Suzhou, 215123 Jiangsu, PR China. E-mail: zqjiang@suda.edu.cn*
[b]*School of Chemistry and Life Sciences, Suzhou University of Science and Technology, Suzhou, 215009 Jiangsu, China*

†Electronic supplementary information (ESI) available. CCDC 2411672 and 2411674. For ESI and crystallographic data in CIF or other electronic format see DOI: https://doi.org/10.1039/d5qo00698h

‡These authors contributed equally to this work.

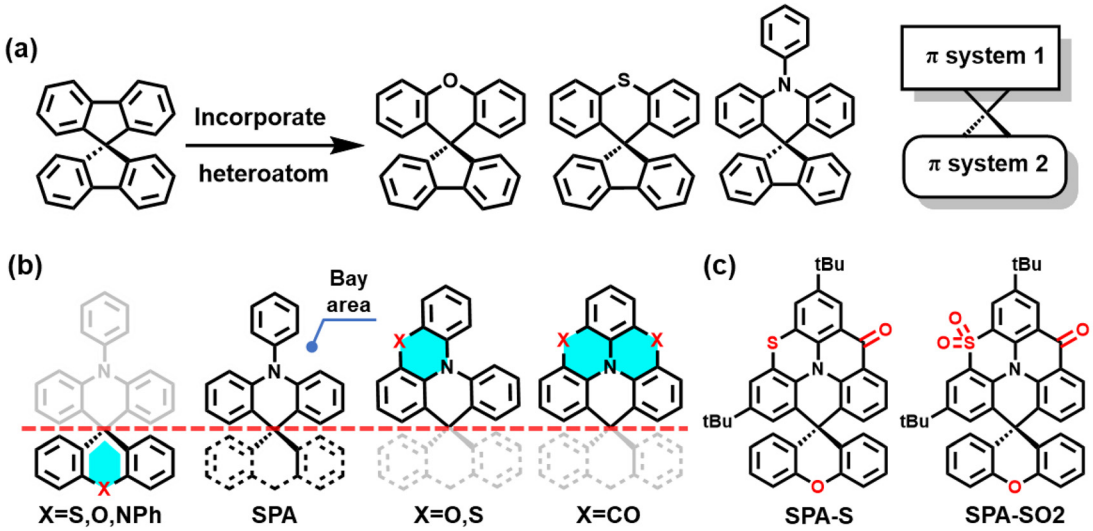

Fig. 1 (a) 9,9′-Spirobifluorene structure and its derivatives, (b) bridging modification of the SPA core, and (c) this work.

together, including single crystal structures, absorption and emission spectra, and electrochemical properties. Experimental and theoretical studies show that oxidizing the bridging sulfur atom alters the electronic structure, leading to a variety of property changes, most notably a blue shift and narrowing of the spectra.[34–36] This clearly illustrates the effectiveness of bridging modifications for molecular design. Finally, we applied SPA-SO2 in electroluminescence devices, achieving deep blue emission at 436 nm with a maximum external quantum efficiency (EQE_{max}) of 9.4%.

2 Results and discussion

The synthetic routes of the two molecules are shown in Scheme 1. Starting from phenothiazine, compound **1** was synthesized *via* Friedel–Crafts alkylation (72% yield), followed by a nucleophilic substitution to afford compound **2** (63% yield).[37] The cyclization of the cyano group with an adjacent benzene ring in the presence of multiple functional groups presents significant synthetic challenges, as it requires careful optimization of both reaction yield and functional group compatibility. Therefore, selecting appropriate synthetic routes and reaction conditions is particularly crucial. Initially, we attempted to hydrolyze the cyano group to a carboxylic acid group, followed by classical Friedel–Crafts acylation. However, compound **2** exhibited poor solubility in polar solvents during hydrolysis, resulting in only trace amounts of the product. We then attempted direct cyclization of the cyano group using highly acidic trifluoromethanesulfonic acid (Scheme S2†).[38] Analysis of nuclear magnetic resonance (NMR) spectra suggested that the sulfur bridge of phenothiazine is preferentially cleaved (Fig. S6†). In our subsequent investigation, we employed diisobutylaluminium hydride to convert the cyano group into the corresponding aldehyde functionality, achieving a high yield of 89%. Then, the Lewis acid catalyzed cycliza-

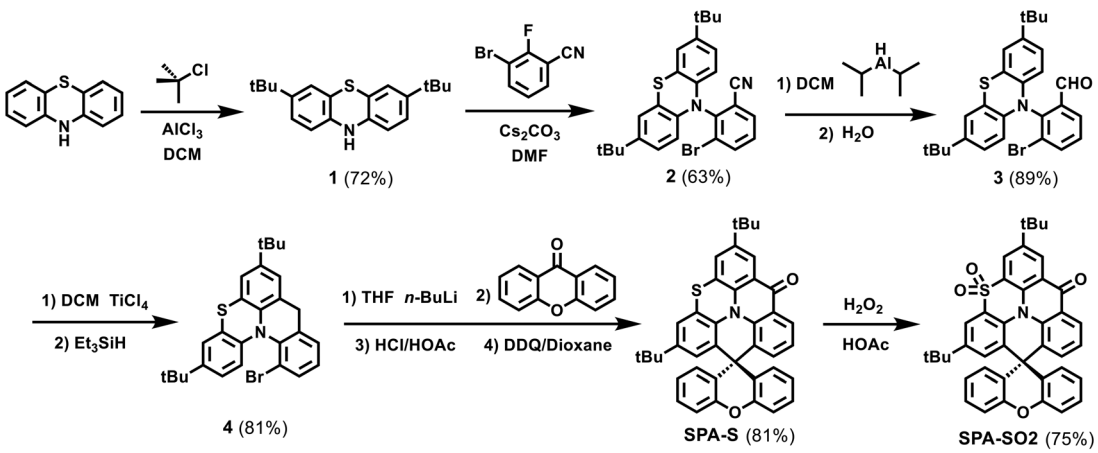

Scheme 1 Synthetic routes for SPA-S and SPA-SO2.

tion–disproportionation process followed by reduction with triethylsilane was successfully used to give compound **4** in 81% yield.[39] Since it does not contain other reactive functional groups that require additional protection reactions, compound **4** can be directly employed in a low-temperature lithium halide exchange reaction and Friedel–Crafts alkylation to form an intermediate with a spiro structure. Simple oxidation of the intermediate with 2,3-dichloro-5,6-dicyano-1,4-benzoquinone (DDQ) gave SPA-S in 81% yield, and further oxidation using a mixture of hydrogen peroxide and acetic acid afforded SPA-SO2 in 75% yield. The target compounds were characterized using NMR and MALDI-TOF.

Single crystals of SPA-S and SPA-SO2 were obtained by diffusion of a solvent mixture of ethanol and dichloromethane. As shown in Fig. 2a, due to the relatively large atomic radius of sulfur, the C–S–C bond lengths in SPA-S and SPA-SO2 molecules are longer than the C–C bond length of 1.40 Å in the benzene ring, measuring 1.74/1.75 Å and 1.73/1.74 Å, respectively.[40,41] This elongation effect leads to the C–S–C bond angle of 100° for both molecules, which deviates from the conventional hexagonal internal angle of 120°. The bond angle deviation of molecules further triggers a slight out-of-plane bending of the located planar structure (Fig. 2b).

The advantage of the rigid spiro structure is that its dihedral angles are almost orthogonal, which tends to increase intermolecular distances and reduce π···π interactions.[32,36] Compared to SPA-S, SPA-SO2 contains more oxygen atoms, leading to more O ···H interactions (Fig. S8†), which further restricts the molecular packing distance, as evidenced by the face-to-face stacking distance of 3.56 Å observed in the packing modes (Fig. 2c). In addition, weak intermolecular interactions can significantly influence the packing arrangement of crystals.[18,40] SPA-S displays weak interactions predominantly in molecular pairs, leading to a regular layered arrangement, while SPA-SO2 molecules experience weak interactions with multiple neighboring molecules, resulting in a more complex packing structure.

We tested the electrochemical properties using cyclic voltammetry (CV) under a nitrogen atmosphere, and the data are shown in Fig. S10.† Estimated from the onsets of oxidation waves, the calculated ionization potential (IP) of SPA-SO2 is −6.00 eV, significantly deeper than that of SPA-S (−5.25 eV). This reflects the strong electron-withdrawing effect of the sulfone group, which stabilizes the HOMO and raises the oxidation potential. Their electron affinities (EA) are similar, −2.70 and −2.88 eV, respectively. These results indicate that the oxidation process predominantly affects the HOMO energy level, while the lowest unoccupied molecular orbital (LUMO) remains largely unaffected. This is attributed to the different spatial distributions of the frontier molecular orbitals, as further discussed in the theoretical calculations section. As the HOMO is distributed over the altered functional groups during the oxidation reaction, the resulting changes are more pronounced, whereas the LUMO is mainly localized on the unchanged carbonyl moieties. Compared with data from the literature reporting the same oxidation phenomenon, the HOMO levels of the products were decreased to different degrees from 0.2 to 0.8 eV (Table S2†).[35,42–44] Consequently, SPA-SO2 has a larger energy gap (E_g) of 3.12 eV compared to the 2.37 eV for SPA-S, indicating its potential for deep blue emission.

The photophysical properties of the two materials were examined, and the pertinent data are presented in Table 1. The absorption and emission spectra of the two molecules in toluene are displayed in Fig. 3. Consistent with previous analyses of electrochemical properties, the different E_g of SPA-S

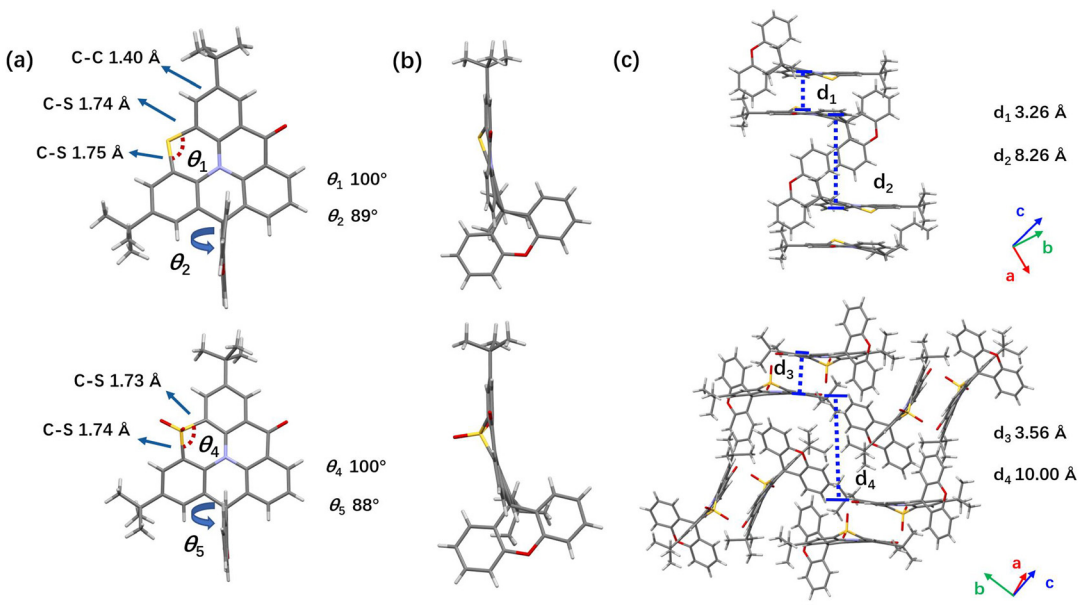

Fig. 2 (a) Top and (b) side view, along with (c) the packing mode of the single crystal structures of (top) SPA-S and (bottom) SPA-SO2.

Table 1 The summary of physical and photophysical properties of SPA-S and SPA-SO2

	IP[a] [eV]	EA[a] [eV]	E_g[b] [eV]	λ_{Abs}[c] [nm]	λ_{Fl}[d] [nm]	FWHM[d] [nm]	$\Delta\lambda$[e] [nm]	E_s[f] [eV]	E_T[g] [eV]	ΔE_{ST}[h] [eV]
SPA-S	−5.25	−2.70	2.55	448	517	60	69	2.57	2.35	0.22
SPA-SO2	−6.00	−2.88	3.12	410	432	34	22	2.95	2.72	0.23

[a] Evaluated from CV curves. [b] E_g = EA − IP. [c] Evaluated from absorption spectra in dilute toluene solution (10^{-5} M, at room temperature). [d] Evaluated from emission spectra in dilute toluene solution (10^{-5} M, at room temperature). [e] Stokes shift, $\Delta\lambda = \lambda_{PL} - \lambda_{Abs}$. [f] Evaluated from fluorescence spectra in frozen toluene (at 77 K). [g] Evaluated from phosphorescence spectra in frozen toluene (at 77 K). [h] $\Delta E_{ST} = E_s - E_T$.

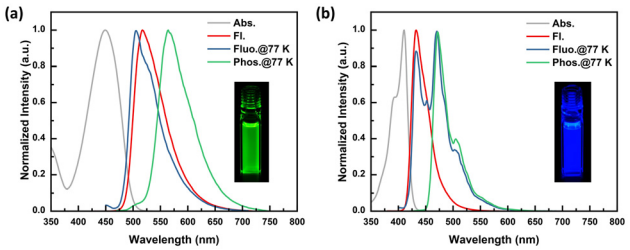

Fig. 3 UV/vis absorption, fluorescence (298 K), fluorescence (77 K), and phosphorescence (77 K) spectra of (a) SPA-S and (b) SPA-SO2 in toluene. Inset: photographs in toluene solution under 365 nm UV light.

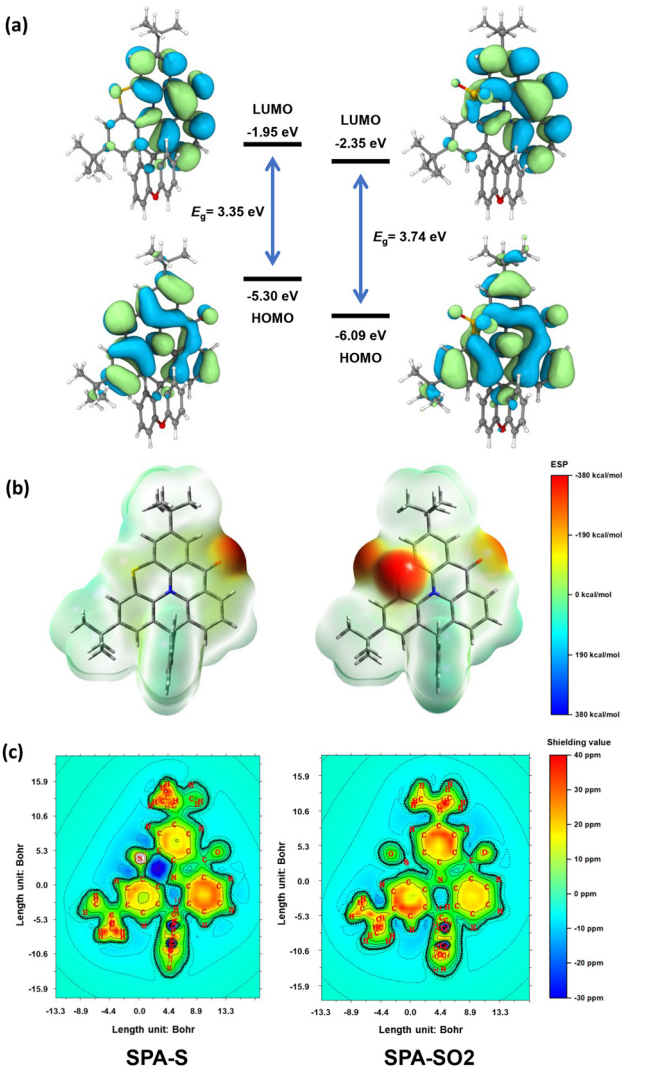

Fig. 4 (a) Frontier molecular orbital distributions and energy levels, (b) electrostatic potential map, and (c) two-dimensional iso-chemical shielding surfaces at 1 Å above the *XY* plane from DFT calculations of SPA-S (left) and SPA-SO2 (right).

and SPA-SO2 causes their absorption peaks to be at 448 and 410 nm, respectively, which are attributed to π–π* and n–π* mixed transitions from the conjugated skeleton.[32,35,36] The emission peak of SPA-S is observed at 517 nm with a large Stokes shift of 69 nm, which is similar to the characteristics of the charge transfer (CT) excited state. However, further studies of the emission spectra in polar solvents confirmed that the S_1 states of SPA-S and SPA-SO2 are locally excited (LE) states. Both of them show slight red shifts and broadening of emission peaks with increasing solvent polarity (Fig. S11 and Table S3†).[36] The SPA-SO2 molecule exhibits deep blue emission at 432 nm in dilute toluene solution, with a much smaller Stokes shift of 22 nm, consistent with the behavior of typical LE states. The emission spectral FWHM values of SPA-S and SPA-SO2 are 60 and 34 nm, suggesting greater vibrational coupling during SPA-S emission, leading to spectral broadening and increased Stokes shift.[35,41] In addition, we studied their spectra at 77 K. It can be seen that low temperature suppresses molecular vibration and rotation, and the Stokes shift of the SPA-S fluorescence spectrum decreases to 57 nm. Using the tangent of the onset peaks of the low-temperature spectra, the $S_1/T_1/\Delta E_{st}$ energy levels for SPA-S were determined as 2.57/2.35/0.22 eV and for SPA-SO2 as 2.95/2.72/0.23 eV, respectively. SAP-SO2 obtained from oxidation exhibits higher singlet and triplet energy levels. The small ΔE_{st} indicates that the two molecules may have thermally activated delayed fluorescence (TADF) properties.[45]

The electronic structures of SPA-S and SPA-SO2 were studied using density functional theory (DFT) at the B3LYP-D3 (BJ)/def2-SVP level using the Gaussian 16 package and subsequently the results were visualized using Multiwfn and VMD software.[46–52] The frontier molecular orbital (FMO) distributions and energy levels were simulated at optimized S_0 geometries (Fig. 4a). On the one hand, the HOMO of SPA-S shows an irregular distribution localized on the nitrogen-containing fused ring plane. The 3p-orbital contribution of the sulfur atom significantly influences the π-electron delocalization across the fused ring through resonance effects. Conversely, the HOMO of SPA-SO2 shows a more symmetric distribution across the fused ring, with the sulfone group disrupting

π-conjugation locally without significantly affecting the rest of the ring system. On the other hand, LUMOs of both molecules display similar distributions, suggesting that the LUMOs are predominantly influenced by the conjugated electron-withdrawing effect of the carbonyl group. Electrostatic potential maps (ESP) reveal that the sulfone group, due to its strongly electron-withdrawing nature, exhibits a highly negative electrostatic potential akin to the carbonyl group (Fig. 4b). However, as the sulfone induces an electron-withdrawing effect primarily through inductive interactions affecting inner σ-orbital energy, the carbonyl group exerts a direct impact on the π-orbitals, leading to its pronounced influence on the LUMO.

We further assessed the aromaticity of the fused rings, which are mainly composed of delocalized π-bonds in the HOMO, by performing two-dimensional iso-chemical shielding surface (2D-ICSS$_{zz}$) analyses (Fig. 4c).[53,54] In the 2D-ICSS$_{zz}$ analysis of SPA-S, both sulfur and nitrogen effectively donate one lone pair of electrons to the conjugated system *via* their p-orbitals, and the embedded six-membered ring exhibits a strong shielding effect (less than −20 ppm), indicative of anti-aromaticity. Neighboring benzene rings experience reduced aromaticity due to the conjugative impact of the sulfur atom, while the benzene rings farthest from the sulfur atom exhibit the highest aromaticity. Focusing on SPA-SO2 molecules, two benzene rings substituted with the *tert*-butyl group in SPA-SO2 display the strongest aromaticity. This is due to the fact that the sulfone group has no 3p-orbital involved in conjugation, effectively separating the π-electron clouds of the adjacent benzene rings, thereby enhancing their aromatic character.

To investigate the reasons for the significant differences in the photophysical properties of the two molecules, time-dependent density functional theory (TD-DFT) calculations were performed to analyze excited state characteristics. The electron–hole distributions confirm that both the first singlet and triplet excited states predominantly arise from HOMO–LUMO transitions (Fig. S13†). Excited state energy levels and related properties were calculated, as detailed in Tables S4 and S5.† We evaluated the root mean square deviation (RMSD) and reorganization energy and determined the values for SPA-S and SPA-SO2 to be 0.415/0.378 Å and 0.458/0.268 eV, respectively (Table S7†). The larger conformational adjustments in SPA-S upon electronic excitation are attributed to the delocalized 3p-orbital electrons of the sulfur atom, which participate in conjugation and increase the polarizability of the system, facilitating electron cloud redistribution under external perturbations. To verify this claim, the bonded and free atomic volumes and contribution of atomic polarizability to the polarized nature of the molecule are calculated. As seen from Fig. S15,† the atomic volumes and atomic polarizations show a high degree of consistency, with the sulfur atom showing a significant decrease in both atomic volume and atomic polarization after oxidation, while the other species of atoms show no significant change. From the microscopic point of view, the oxidation of sulfur results in a higher oxidation state and a diminished electron cloud density, thus reducing the atomic volumes and polarization rate contribution.

The theoretical analysis of SPA-S and SPA-SO2 allows us to reasonably explain the effect of bridging modifications of SPA derivatives on their photophysical behavior. The 3p-orbitals of the sulfur increase the HOMO energy level and polarisability of the molecule. This results in SPA-S exhibiting a lower excited state energy level, higher reorganization energy, and stronger vibronic coupling during electron transition, as reflected in its red-shifted spectra and broader FWHM. On oxidation of sulfur to sulfone, these detrimental effects are mitigated, resulting in a pronounced blue shift and narrower FWHM.

In the field of organic light-emitting diodes, the oxidation of thioxanthene within bridged structures forming dioxothioxanthene often results in a range of desirable properties, including modulation of molecular vibrations and tunability of molecular emission colors.[35,36,42] Building on our previous discussion, we decided to apply SPA-SO2 in electroluminescence devices. First, we investigated the photophysical properties (Fig. S16†) and exciton dynamics (Table S11†) of solid films. In the host–guest doped state, the film spectra remained largely unchanged from those of the solution state, with a PLQY of 58.5%. The temperature-dependent decay curves (Fig. S17†) confirmed the TADF mechanism of SPA-SO2, with prompt fluorescence and delayed fluorescence lifetimes of 1.57 ns and 19.5 μs, respectively. Devices were further fabricated with the following multilayer structure: ITO/HAT-CN (10 nm)/TAPC (40 nm)/TCTA (10 nm)/mCP (10 nm)/PPF: SPA-SO2 (20 nm)/PPF (5 nm)/TmPyPB (35 nm)/Liq (2 nm)/Al (80 nm). We used ITO as the anode, 1,4,5,8,9,11-hexaazatriphenylenehexacarbonitrile (HAT-CN) as the hole injection layer, 1,1-bis[(di-4-tolylamino)phenyl]cyclohexane (TAPC) as the hole transport layer, tris(4-carbazoyl-9ylphenyl)amine (TCTA) and 1,3-di(9*H*-carbazol-9-yl)benzene (mCP) as the electron-blocking layer, 2,8-bis(diphenylphosphoryl)dibenzo[*b*,*d*]furan (PPF) as the host and hole-blocking layer, 1,3,5-tri(*m*-pyridin-3-ylphenyl)benzene (TmPyPB) as the hole-transporting layer, lithium-8-hydroxyquinolinolate (Liq) as the electron injection layer, and Al as the cathode, respectively. The choice of PPF as the host is motivated by its high triplet state which matches the excited state energy level of the guest for better energy transfer. Relevant information is summarized in Fig. 5a and b.

As shown in Fig. 5c, the device achieved deep blue electroluminescence at 436 nm with a FWHM of 52 nm at 1 wt% doping concentration. At the same doping concentration, SPA-SO2 demonstrated an EQE$_{max}$ of 9.4% and power efficiency of 3.05 lm W^{-1}. It should be noted that the compound QPO, obtained by dual bridging of triphenylamine using sulfone and carbonyl modifications, has an electroluminescence efficiency of only 2.5% EQE$_{max}$.[38] Benefiting from the spatial site-barrier modification of the spiro structure that inhibits the interactions between the guest molecules, the device efficiency remains consistent at different doping concentrations (Fig. 5d). In addition, we compared the differences in charge transport capability between SPA-S and SPA-SO2. We tested the voltage–current density curves of SPA-S and SPA-SO2 with the same device structure (Fig. S20†). SPA-SO2 exhibits a

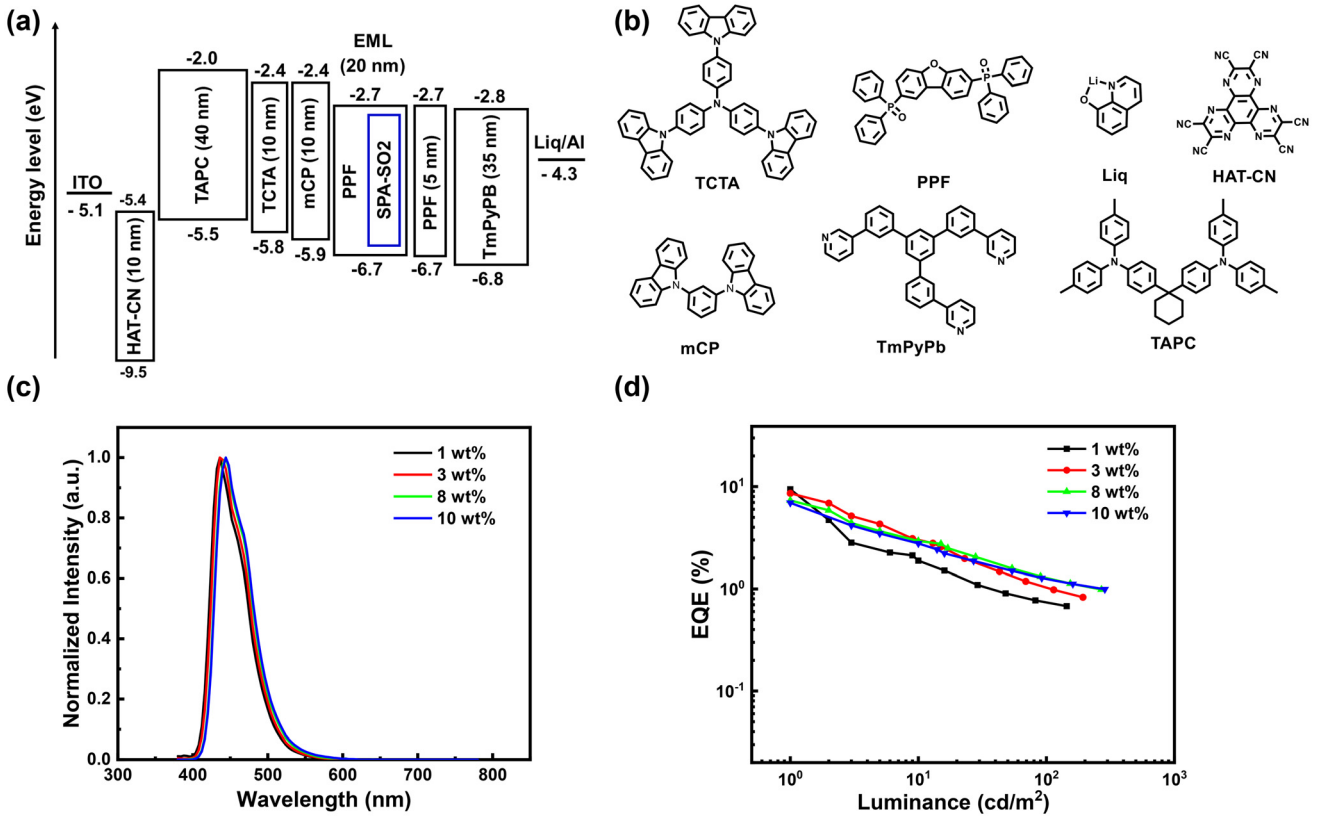

Fig. 5 (a) Energy level alignment of the device, (b) molecular structures of materials in different layers, and characteristics of devices based on SPA-SO2 illustrated by (c) EL spectra and (d) EQE–luminance curves recorded at different doping ratios.

higher current density at the same voltage, indicating better charge transport capability. This may be attributed to the greater rigidity of the SPA-SO2 molecule with fewer geometrical changes and smaller reorganization energies during carrier injection and transport, which are favorable for charge transport. This corresponds to the conclusions from the theoretical calculations. Given the aforementioned, we firmly believe that SPA-SO2 could be a viable and reliable candidate for electroluminescence materials.

3 Conclusions

In summary, through fully bridging sulfone, carbonyl, and oxygen on the SPA core, we synthesized SPA-SO2. Characterization of properties showed that its precursor SPA-S exhibits green emission at 517 nm with an FWHM of 60 nm, while SPA-SO2 exhibits deep blue emission at 432 nm with an FWHM of 34 nm. Oxidation localizes sulfur outer electrons, leading to pronounced spectral blue shifting and narrowing. It revealed that the delocalized 3p electrons of sulfur lead to spectral broadening. Theoretical calculations provided mechanistic insights, confirming that bridging modifications directly impact the electronic structure and photophysical properties. Subsequently, the SPA-SO2 molecule was applied in electroluminescence devices, where it maintained deep blue emission at 436 nm and achieved an EQE_{max} of 9.4%. These findings offer valuable guidance for designing SPA compounds and highlight the potential of bridging modifications in tuning optical and electronic properties for advanced optoelectronic materials.

Author contributions

Shi-Jie Ge performed the experiments and wrote the manuscript under the guidance of Zuo-Quan Jiang and Dong-Ying Zhou. Yue-Jian Yang, Rui-Hong Liu, You-Jun Yu, Rehman Mehvish Abdul, Hai-Xiao Jiang, and Wei Gao contributed to the data curation and experimental discussion. Funding acquisition was done by Zuo-Quan Jiang.

Conflicts of interest

The authors declare no conflict of interest.

Data availability

The data supporting this article have been included as part of the ESI.†

Acknowledgements

The authors acknowledge financial findings from the National Natural Science Foundation of China (Nos. 22175124 and 62175171), and the Natural Science Foundation of Jiangsu Province of China (BK20220057). This work is also supported by Collaborative Innovation Center of Suzhou Nano Science & Technology, the 111 Project, Joint International Research Laboratory of Carbon-Based Functional Materials and Devices, Suzhou Key Laboratory of Functional Nano & Soft Materials.

References

1 T. P. I. Saragi, T. Spehr, A. Siebert, T. Fuhrmann-Lieker and J. Salbeck, Spiro Compounds for Organic Optoelectronics, *Chem. Rev.*, 2007, **107**, 1011–1065.
2 S.-Y. Yang, J. Wang, Z. Deng, Y. Xu, X. Su, L. Zhang, S. Yang, R. T. Kwok, J. W. Lam and B. Z. Tang, Spiro-Materials with Aggregation-Induced Emission, *Matter*, 2024, **7**, 3390–3421.
3 M. Rajasekar, Spirobifluorene Derivatives and Their Biomaterial Applications: Current Trends, *J. Mol. Struct.*, 2022, **1255**, 132406.
4 K. Song, Y. Zhang, S. Wu, S. Yang, S. Wei, S. Chen, H. Ito, K. Itami and Y. Li, Spiro-Fused Dibenzo[*g*, *p*]Chrysene: Annulative π-Extension (APEX) Synthesis and Properties, *Org. Chem. Front.*, 2025, **12**, 2225–2231.
5 Y. Tao, K. Yuan, T. Chen, P. Xu, H. Li, R. Chen, C. Zheng, L. Zhang and W. Huang, Thermally Activated Delayed Fluorescence Materials Towards the Breakthrough of Organoelectronics, *Adv. Mater.*, 2014, **26**, 7931–7958.
6 X. Cai and S.-J. Su, Marching Toward Highly Efficient, Pure-Blue, and Stable Thermally Activated Delayed Fluorescent Organic Light-Emitting Diodes, *Adv. Funct. Mater.*, 2018, **28**, 1802558.
7 C. Poriel and J. Rault-Berthelot, Dihydroindenofluorene Positional Isomers, *Acc. Chem. Res.*, 2018, **51**, 1818–1830.
8 S. Liu, D. Xia and M. Baumgarten, Rigidly Fused Spiro-Conjugated π-Systems, *ChemPlusChem*, 2021, **86**, 36–48.
9 M. Bhanuchandra, H. Yorimitsu and A. Osuka, Synthesis of Spirocyclic Diarylfluorenes by One-Pot Twofold SN Ar Reactions of Diaryl Sulfones with Diarylmethanes, *Org. Lett.*, 2016, **18**, 384–387.
10 K. Nogi and H. Yorimitsu, Aromatic Metamorphosis: Conversion of an Aromatic Skeleton into a Different Ring System, *Chem. Commun.*, 2017, **53**, 4055–4065.
11 F. Lucas, O. A. Ibraikulov, C. Quinton, L. Sicard, T. Heiser, D. Tondelier, B. Geffroy, N. Leclerc, J. Rault-Berthelot and C. Poriel, Spirophenylacridine-2,7-(Diphenylphosphineoxide)-Fluorene: A Bipolar Host for High-Efficiency Single-Layer Blue Phosphorescent Organic Light-Emitting Diodes, *Adv. Opt. Mater.*, 2020, **8**, 1901225.
12 S. Thiery, D. Tondelier, B. Geffroy, O. Jeannin, J. Rault-Berthelot and C. Poriel, Modulation of the Physicochemical Properties of Donor–Spiro–Acceptor Derivatives through Donor Unit Planarisation: Phenylacridine versus Indoloacridine—New Hosts for Green and Blue Phosphorescent Organic Light-Emitting Diodes (PhOLEDs), *Chem. – Eur. J.*, 2016, **22**, 10136–10149.
13 Z. Jiang, Z. Liu, C. Yang, C. Zhong, J. Qin, G. Yu and Y. Liu, Multifunctional Fluorene-Based Oligomers with Novel Spiro-Annulated Triarylamine: Efficient, Stable Deep-Blue Electroluminescence, Good Hole Injection, and Transporting Materials with Very High T_g, *Adv. Funct. Mater.*, 2009, **19**, 3987–3995.
14 Y.-K. Wang, S.-F. Wu, Y. Yuan, S.-H. Li, M.-K. Fung, L.-S. Liao and Z.-Q. Jiang, Donor-σ-Acceptor Molecules for Green Thermally Activated Delayed Fluorescence by Spatially Approaching Spiro Conformation, *Org. Lett.*, 2017, **19**, 3155–3158.
15 Y.-K. Qu, Q. Zheng, J. Fan, L.-S. Liao and Z.-Q. Jiang, Spiro Compounds for Organic Light-Emitting Diodes, *Acc. Mater. Res.*, 2021, **2**, 1261–1271.
16 R.-H. Liu, M.-T. Li, Y.-J. Yang, S.-J. Ge, Z.-H. Qu, Z.-Q. Feng, Y. Wang, Z.-H. Yu, D.-Y. Zhou, C. Zhong, L.-S. Liao and Z.-Q. Jiang, Efficiency Boost in Through Space Charge Transfer Emitters: Insights from Spiro Lateral Rocking Confinement, *Adv. Mater.*, 2025, **37**, 2415951.
17 C.-Y. Chan, Y.-C. Wong, M.-Y. Chan, S.-H. Cheung, S.-K. So and V. W.-W. Yam, Bifunctional Heterocyclic Spiro Derivatives for Organic Optoelectronic Devices, *ACS Appl. Mater. Interfaces*, 2016, **8**, 24782–24792.
18 M. Romain, D. Tondelier, B. Geffroy, O. Jeannin, E. Jacques, J. Rault-Berthelot and C. Poriel, Donor/Acceptor Dihydroindeno[1,2- *a*]Fluorene and Dihydroindeno[2,1- *b*] Fluorene: Towards New Families of Organic Semiconductors, *Chem. – Eur. J.*, 2015, **21**, 9426–9439.
19 Y. Chen, J. Xu and P. Gao, A Route to Carbon-sp^3 Bridging Spiro-Molecules: Synthetic Methods and Optoelectronic Applications, *Org. Chem. Front.*, 2024, **11**, 508–539.
20 T.-A. Lin, T. Chatterjee, W.-L. Tsai, W.-K. Lee, M.-J. Wu, M. Jiao, K.-C. Pan, C.-L. Yi, C.-L. Chung, K.-T. Wong and C.-C. Wu, Sky-Blue Organic Light Emitting Diode with 37% External Quantum Efficiency Using Thermally Activated Delayed Fluorescence from Spiroacridine-Triazine Hybrid, *Adv. Mater.*, 2016, **28**, 6976–6983.
21 J. Lee, N. Aizawa, M. Numata, C. Adachi and T. Yasuda, Versatile Molecular Functionalization for Inhibiting Concentration Quenching of Thermally Activated Delayed Fluorescence, *Adv. Mater.*, 2017, **29**, 1604856.
22 G. Méhes, H. Nomura, Q. Zhang, T. Nakagawa and C. Adachi, Enhanced Electroluminescence Efficiency in a Spiro-Acridine Derivative through Thermally Activated Delayed Fluorescence, *Angew. Chem., Int. Ed.*, 2012, **51**, 11311–11315.
23 X. Tang, L.-S. Cui, H.-C. Li, A. J. Gillett, F. Auras, Y.-K. Qu, C. Zhong, S. T. E. Jones, Z.-Q. Jiang, R. H. Friend and L.-S. Liao, Highly Efficient Luminescence from Space-Confined Charge-Transfer Emitters, *Nat. Mater.*, 2020, **19**, 1332–1338.
24 X.-D. Zhu, X.-J. Ma, Y.-K. Wang, Y. Li, C.-H. Gao, Z.-K. Wang, Z.-Q. Jiang and L.-S. Liao, Hole-Transporting Materials Incorporating Carbazole into Spiro-Core for

Highly Efficient Perovskite Solar Cells, *Adv. Funct. Mater.*, 2019, **29**, 1807094.

25 Y.-K. Wang, Z.-C. Yuan, G.-Z. Shi, Y.-X. Li, Q. Li, F. Hui, B.-Q. Sun, Z.-Q. Jiang and L.-S. Liao, Dopant-Free Spiro-Triphenylamine/Fluorene as Hole-Transporting Material for Perovskite Solar Cells with Enhanced Efficiency and Stability, *Adv. Funct. Mater.*, 2016, **26**, 1375–1381.

26 D. Hellwinkel and M. Melan, Heteropolycyclen Vom Triangulen-Typ, II. Zur Stereochemie Verbrückter Triarylamine, *Chem. Ber.*, 1974, **107**, 616–626.

27 Z. Fang, T.-L. Teo, L. Cai, Y.-H. Lai, A. Samoc and M. Samoc, Bridged Triphenylamine-Based Dendrimers: Tuning Enhanced Two-Photon Absorption Performance with Locked Molecular Planarity, *Org. Lett.*, 2009, **11**, 1–4.

28 J. Borstelmann, V. Gensch, D. Fehn, M. E. Miehlich, F. Hampel, F. Rominger, K. Meyer and M. Kivala, A Trithia-Bridged N -Heterotriangulene: The Hitherto Missing Electron Donor, *Angew. Chem., Int. Ed.*, 2025, **64**, e202423802.

29 S.-N. Zou, C.-C. Peng, S.-Y. Yang, Y.-K. Qu, Y.-J. Yu, X. Chen, Z.-Q. Jiang and L.-S. Liao, Fully Bridged Triphenylamine Derivatives as Color-Tunable Thermally Activated Delayed Fluorescence Emitters, *Org. Lett.*, 2021, **23**, 958–962.

30 Y.-K. Wang, Q. Sun, S.-F. Wu, Y. Yuan, Q. Li, Z.-Q. Jiang, M.-K. Fung and L.-S. Liao, Thermally Activated Delayed Fluorescence Material as Host with Novel Spiro-Based Skeleton for High Power Efficiency and Low Roll-Off Blue and White Phosphorescent Devices, *Adv. Funct. Mater.*, 2016, **26**, 7929–7936.

31 C. Poriel, J. Rault-Berthelot, S. Thiery, C. Quinton, O. Jeannin, U. Biapo, D. Tondelier and B. Geffroy, 9 *H* -Quinolino[3,2,1- *k*]Phenothiazine: A New Electron-Rich Fragment for Org. Electron., *Chem. – Eur. J.*, 2016, **22**, 17930–17935.

32 Y.-J. Yu, Z.-Q. Feng, X.-Y. Meng, L. Chen, F.-M. Liu, S.-Y. Yang, D.-Y. Zhou, L.-S. Liao and Z.-Q. Jiang, Introducing Spiro-locks into the Nitrogen/Carbonyl System towards Efficient Narrowband Deep-blue Multi-resonance TADF Emitters, *Angew. Chem., Int. Ed.*, 2023, **62**, e202310047.

33 H.-J. Tan, J.-R. Yu, Z.-Z. Lin, G.-X. Yang, Z.-Q. Long, Y.-L. Deng, Z.-L. Zhu, X.-K. Chen, J.-X. Jian, Q.-X. Tong and C.-S. Lee, The Role of a Small Molecular Dipole Moment for Efficient Non-Doped Deep Blue Thermally Activated Delayed Fluorescence Emitters, *Chem. Eng. J.*, 2024, **481**, 148567.

34 G. Zhu, Y. Song, Q. Zhang, W. Ding, X. Chen, Y. Wang and G. Zhang, Modulating the Properties of Buckybowls Containing Multiple Heteroatoms, *Org. Chem. Front.*, 2021, **8**, 727–735.

35 S. Jiang, Y. Yu, D. Li, Z. Chen, Y. He, M. Li, G.-X. Yang, W. Qiu, Z. Yang, Y. Gan, J. Lin, Y. Ma and S.-J. Su, Sulfone-Embedded Heterocyclic Narrowband Emitters with Strengthened Molecular Rigidity and Suppressed High-Frequency Vibronic Coupling, *Angew. Chem., Int. Ed.*, 2023, **62**, e202218892.

36 S. Jiang, D. Liu, Z. Chen, Z. Yang, Y. He, G.-X. Yang, D. Li and S.-J. Su, Carbonyl-Based Narrowband Emitters Peripherally Decorated by Sulfone-Containing Spiro Structures, *Adv. Funct. Mater.*, 2024, **34**, 2316355.

37 G. Sych, R. Pashazadeh, Y. Danyliv, O. Bezvikonnyi, D. Volyniuk, A. Lazauskas and J. V. Grazulevicius, Reversibly Switchable Phase-Dependent Emission of Quinoline and Phenothiazine Derivatives towards Applications in Optical Sensing and Information Multicoding, *Chem. – Eur. J.*, 2021, **27**, 2826–2836.

38 S.-Y. Yang, Q.-S. Tian, X.-J. Liao, Z.-G. Wu, W.-S. Shen, Y.-J. Yu, Z.-Q. Feng, Y.-X. Zheng, Z.-Q. Jiang and L.-S. Liao, Efficient Circularly Polarized Thermally Activated Delayed Fluorescence Hetero-[4]Helicene with Carbonyl-/Sulfone-Bridged Triarylamine Structures, *J. Mater. Chem. C*, 2022, **10**, 4393–4401.

39 Z. Shi, S. Chen, Q. Xiao and D. Yin, Formation and Disproportionation of Xanthenols to Xanthenes and Xanthones and Their Use in Synthesis, *J. Org. Chem.*, 2021, **86**, 3334–3343.

40 C. Poriel, J. Rault-Berthelot and D. Thirion, Modulation of the Electronic Properties of 3π-2spiro Compounds Derived from Bridged Oligophenylenes: A Structure–Property Relationship, *J. Org. Chem.*, 2013, **78**, 886–898.

41 C. Cao, J.-H. Tan, Z.-L. Zhu, J.-D. Lin, H.-J. Tan, H. Chen, Y. Yuan, M.-K. Tse, W.-C. Chen and C.-S. Lee, Intramolecular Cyclization: A Convenient Strategy to Realize Efficient BT.2020 Blue Multi-Resonance Emitter for Organic Light-Emitting Diodes, *Angew. Chem., Int. Ed.*, 2023, **62**, e202215226.

42 T. Hua, J. Miao, H. Xia, Z. Huang, X. Cao, N. Li and C. Yang, Sulfone-Incorporated Multi-Resonance TADF Emitter for High-Performance Narrowband Blue OLEDs with EQE of 32%, *Adv. Funct. Mater.*, 2022, **32**, 2201032.

43 Y. Zhang, M. Chen, X. Wang, M. Lin, H. Wang, W. Li, F. Chen, Q. Liao, H. Chen, Q. Chen, M. Lin and H. Yang, Efficient and Fast X-Ray Luminescence in Organic Phosphors Through High-Level Triplet-Singlet Reverse Intersystem Crossing, *CCS Chem.*, 2024, **6**, 334–341.

44 Z. Liu, W. Han, J. Lan, L. Sun, J. Tang, C. Zhang and J. You, Molecular Engineering of Chalcogen-Embedded Anthanthrenes via Peri-Selective C-H Activation: Fine-Tuning of Crystal Packing for Organic Field-Effect Transistors, *Angew. Chem., Int. Ed.*, 2023, **62**, e202211412.

45 Y. Yuan, X. Tang, X.-Y. Du, Y. Hu, Y.-J. Yu, Z.-Q. Jiang, L.-S. Liao and S.-T. Lee, The Design of Fused Amine/Carbonyl System for Efficient Thermally Activated Delayed Fluorescence: Novel Multiple Resonance Core and Electron Acceptor, *Adv. Opt. Mater.*, 2019, **7**, 1801536.

46 C. Adamo and V. Barone, Toward Reliable Density Functional Methods without Adjustable Parameters: The PBE0 Model, *J. Chem. Phys.*, 1999, **110**, 6158–6170.

47 F. Weigend and R. Ahlrichs, Balanced Basis Sets of Split Valence, Triple Zeta Valence and Quadruple Zeta Valence Quality for H to Rn: Design and Assessment of Accuracy, *Phys. Chem. Chem. Phys.*, 2005, **7**, 3297.

48 F. Weigend, Accurate Coulomb-fitting Basis Sets for H to Rn, *Phys. Chem. Chem. Phys.*, 2006, **8**, 1057.
49 S. Grimme, S. Ehrlich and L. Goerigk, Effect of the Damping Function in Dispersion Corrected Density Functional Theory, *J. Comput. Chem.*, 2011, **32**, 1456–1465.
50 M. J. Frisch, G. W. Trucks, H. B. Schlegel, G. E. Scuseria, M. A. Robb, J. R. Cheeseman, G. Scalmani, V. Barone, G. A. Petersson, H. Nakatsuji, X. Li, M. Caricato, A. V. Marenich, J. Bloino, B. G. Janesko, R. Gomperts, B. Mennucci, H. P. Hratchian, J. V. Ortiz, A. F. Izmaylov, J. L. Sonnenberg, D. Williams-Young, F. Ding, F. Lipparini, F. Egidi, J. Goings, B. Peng, A. Petrone, T. Henderson, D. Ranasinghe, V. G. Zakrzewski, J. Gao, N. Rega, G. Zheng, W. Liang, M. Hada, M. Ehara, K. Toyota, R. Fukuda, J. Hasegawa, M. Ishida, T. Nakajima, Y. Honda, O. Kitao, H. Nakai, T. Vreven, K. Throssell, J. A. Montgomery Jr., J. E. Peralta, F. Ogliaro, M. J. Bearpark, J. J. Heyd, E. N. Brothers, K. N. Kudin, V. N. Staroverov, T. A. Keith, R. Kobayashi, J. Normand, K. Raghavachari, A. P. Rendell, J. C. Burant, S. S. Iyengar, J. Tomasi, M. Cossi, J. M. Millam, M. Klene, C. Adamo, R. Cammi, J. W. Ochterski, R. L. Martin, K. Morokuma, O. Farkas, J. B. Foresman and D. J. Fox, *Gaussian 16 Revision C.02*, 2016, Gaussian Inc., Wallingford CT.
51 W. Humphrey, A. Dalke and K. Schulten, VMD: Visual Molecular Dynamics, *J. Mol. Graphics*, 1996, **14**, 33–38.
52 T. Lu and F. Chen, Multiwfn: A Multifunctional Wavefunction Analyzer, *J. Comput. Chem.*, 2012, **33**, 580–592.
53 S. Klod and E. Kleinpeter, Ab Initio Calculation of the Anisotropy Effect of Multiple Bonds and the Ring Current Effect of Arenes—Application in Conformational and Configurational Analysis, *J. Chem. Soc., Perkin Trans. 2*, 2001, 1893–1898.
54 Z. Liu, T. Lu and Q. Chen, An Sp-Hybridized All-Carboatomic Ring, Cyclo[18]Carbon: Bonding Character, Electron Delocalization, and Aromaticity, *Carbon*, 2020, **165**, 468–475.